Article

New Methodology for Shoreline Extraction Using Optical and Radar (SAR) Satellite Imagery

Sara Zollini [1,*], Donatella Dominici [1,*], Maria Alicandro [1,*], María Cuevas-González [2], Eduard Angelats [2], Francesca Ribas [3] and Gonzalo Simarro [4]

[1] DICEAA—Department of Civil, Construction-Architectural and Environmental Engineering, University of L'Aquila, Via G. Gronchi 18, 67100 L'Aquila, Italy

[2] Geomatics Research Unit, Centre Tecnològic de Telecomunicacions de Catalunya (CTTC/CERCA), Av. Carl Friedrich Gauss 7, 08860 Castelldefels, Spain

[3] Department of Physics, Universitat Politècnica de Catalunya, C. Jordi Girona 1-3, 08034 Barcelona, Spain

[4] Department of Marine Geosciences, Instituto de Ciencias del Mar (ICM-CSIC), Passeig Maritim de la Barceloneta 37-49, 08003 Barcelona, Spain

* Correspondence: sara.zollini@univaq.it (S.Z.); donatella.dominici@univaq.it (D.D.); maria.alicandro@univaq.it (M.A.); Tel.: +39-0862-434116 (S.Z.)

Abstract: Coastal environments are dynamic ecosystems, constantly subject to erosion/accretion processes. Erosional trends have unfortunately been intensifying for decades due to anthropic factors and an accelerated sea level rise might exacerbate the problem. It is crucial to preserve these areas for safeguarding not only coastal ecosystems and cultural heritage, but also the population living there. In this context, monitoring coastal areas is essential and geomatics techniques, especially satellite remote sensing imagery, might prove very advantageous. In this paper, a semi-automatic methodology to extract shorelines from SAR (Synthetic Aperture Radar) Sentinel-1 and optical Sentinel-2 satellite images was developed. An experimental algorithm, called J-Net Dynamic, was tested in two pilot sites. The semi-automatic methodology was validated with GNSS (Global Navigation Satellite System) reference shorelines and demonstrated to be a powerful tool for a robust extraction of the shoreline both from optical and SAR images. The experimental algorithm was able to extract the shoreline closer to the reference with SAR images on the natural beach of Castelldefels and it was demonstrated to be less sensitive to speckle effects than the commonly used Canny Edge Detector. Using the SAR images of the urban beach of Somorrostro, the Canny detector was not able to extract the shoreline, while the new algorithm could do it but with low accuracy because of the noise induced by man-made structures. For further investigation, the Sentinel-2-extracted shorelines were also compared to the ones extracted by a state-of-the-art tool, CoastSat, in the two beaches using both automatic and manual thresholds. The mean errors obtained with J-Net Dynamic were generally higher than the ones from CoastSat using the manual threshold but lower if using the automatic one. The proposed methodology including the J-Net Dynamic algorithm proves to extract the shorelines closer to the reference in most of the cases and offers the great advantage of being able to work with both optical and SAR images. This feature could allow to reduce the time lag between satellite derived shorelines paving the way to an enhanced monitoring and management of coastal areas.

Keywords: remote sensing; synthetic aperture radar (SAR); multispectral images; coastal erosion; shoreline extraction; satellite images; canny edge detection; CoastSat; active connection matrix (ACM); GNSS

1. Introduction and State of the Art

The coastal zone represents one of the most populated and developed areas in the world [1]. It has rich biodiversity and more than 45% of world's population lives there [2]. It has always been the subject of human attraction because of their resources, starting from economic reasons, as it includes the main access points to marine trade and transport, to cultural activities and cultural heritage. For these reasons, coastal zones have been growing and

developing continuously and their utilisation has greatly increased during recent decades [3]. This led inevitably to many changes in the coastal environment not only from the point of view of the appearance, but also of the biodiversity of the entire ecosystem. The coastal zone is, at the same time, a vulnerable environment. The hazards, such as hurricanes, storms and tsunami, represent significant threats to the population, infrastructure and to the environment itself. There are also other hazards which are not visible or produce long-term effects, such as rising sea levels and coastal erosion. According to some authors [4,5], global mean sea level has risen about 20 cm since 1880 and this process is accelerating. It was of 1.4 mm per year throughout most of the twentieth century increasing to 3.6 mm per year in 2006–2015. Even if the world follows a low CO_2 emission trend, the global sea level will likely rise at least 0.3 m by 2100. On the contrary, if it follows a pathway with high emissions, a worst-case scenario of as much as 1.1 m by 2100 is possible [4].

The water level is rising mostly because of a combination of meltwater from glaciers and ice sheets and thermal expansion of seawater as it warms [5]. Sea level rise during the 21st century will increase inundation episodes and erosion processes [4]. The latter implies a natural displacement of sand from the dry beach in the offshore direction into deeper waters or in the alongshore direction into other coastal stretches. It can be caused by natural factors such as storms or sea level rise or for anthropogenic reasons, mainly related to the construction of dams in rivers (limiting sediment availability) and of infrastructures in the coastal zone. Other factors such as accelerated urbanization and intensive economic and tourist activities also play a role.

A global and consistent evaluation of coastal morphodynamics over 32 years, from 1984 to 2015, based on satellite observations was studied in [6]. The authors used more than 2 million virtual transects in the coastal active zone to estimate the land losses and gains. The coastal active zone is the most dynamic part of the coast and it is defined as the buffer area between permanent land and water. They demonstrated that the overall surface of eroded permanent land is almost 28,000 km^2, twice the surface of gained land over the same period. This erosive trend is observed not only globally but also at the European level, with nearly all its coasts suffering from an erosive trend. The Mediterranean littoral is the most affected one and, in particular, about 60% of the Catalan coast shows an erosive trend [7].

Prevention has a central role in the management of coastal areas. The protection of coastal green belts as well as the shoreline through nourishments, coastal dykes or other hard infrastructures should be based on a carefully performed risk analysis [8]. Coastal monitoring is essential for the preservation of these areas [2]. Shoreline extraction is included in the so-called "softer" components and this is one of the most used technique for coastal management.

The definition of "shoreline" is a topic of debate. It is the line that delimits a natural body of water. It differs from coastline, which is a strip of land of indefinite length and width that extends inland starting from the shoreline [9]. The main problem of its definition concerns its dynamic nature, so the term "instantaneous shoreline" is more appropriate because it clarifies that it is taken in a specific instant of time. By comparing the instantaneous shorelines taken in different moments, it is possible to monitor the dynamics of coastal areas. Several geomatic techniques have been used for this purpose. Up to now, the simple visual interpretation was generally used but, recently, topographic data collection, photogrammetry, digital image processing techniques, satellite and video remote sensing have been considered valid methods to detect shoreline objectively [10–17]. Satellite images are complementary to video and photogrammetric aerial-based monitoring, and are used to generate shorelines at regional, national or global scales with high temporal frequency (few days). However, they are particularly advantageous compared with traditional and photogrammetric aerial acquisitions. Although they only capture the instantaneous shoreline and the spatial resolution could be a limitation to study small variations, they have the following benefits: they can investigate a wider area, they do not need an "ad hoc" flight to be planned, the data can be acquired and processed more quickly offering a high level of detail, multispectral bands facilitate the delineation of the water and boundary interface, the satellite revisit times are very short and,

finally, there is no need to go physically to the place under investigation. The satellite-derived shorelines could be a tool in the forthcoming years to assess the long-term sustainability of coastal areas, to evaluate the coastal retreat due to sea level rise or to evaluate the lifespan of sand nourishments [18]. The requirements for shoreline delineation depend on the characteristics of the purpose of the study. For this reason, specific investigation methodologies have to satisfy different requirements, e.g., spatial resolution and shoreline position accuracy (from tens of metres to sub-metre), temporal and spatial scales of investigation (e.g., long- or medium-term analyses, regional or local scale), and temporal frequency and response time for up-to-date information [19]. Recently, there has been a growing interest in extracting shoreline from satellite thanks to the deployment of Sentinel-2 (S2) satellites and to Planetscope (Cubesat satellite) with a good spatial and temporal resolution [18]. The Copernicus data (Sentinel-1 (S1) and -2) are used in various fields such as ice monitoring [20], oil-spill monitoring [21], ship detection for maritime security [22], mapping for forest, water and soil management [23–25], ground deformation caused by landslide or earthquake [26], land monitoring [27], emergency management and security [28], agriculture [29,30], but they are also widely exploited in coastal environment and shoreline extraction [13,31–33]. Satellite-derived shorelines, despite being less accurate than other techniques, have the enormous advantage of being weekly available within all our planet. At the same time, some available open-source tools that allow any user to extract shorelines (Coastsat [34] and CASSIE [35]) from S2 imagery have appeared. Shorelines can be extracted also from SAR (Synthetic Aperture Radar) Sentinel-1 (S1) images but generally, the approach is not so straightforward as for S2 imagery, mostly due to the difficulty of interpreting and processing the data. This may explain why the shoreline extraction from SAR images is not so well adopted within the scientific community. A recent review [18] pointed out that shoreline can be extracted from multispectral satellite imagery (Sentinel-2 and Landsat 8), using several water indices and approaches, with an accuracy between 10 and 15 m. Recent studies show that shorelines with sub-pixel accuracy can be extracted in micro-tidal beaches [36], but also in embayed and open-ocean beaches (including different tidal ranges) [37], using several water indices (NDWI, MNDWI, AWEI, WI). Among them, the Normalized Difference Water Index (NDWI) [38] and some of its variants such as the Modified (M) NDWI [39], and used in Coastsat [40], are a key element in any workflow or tool devoted to shoreline extraction [37]. Other water indices such as Automated Water Extraction Index (AWEI) [41] or Water Index (WI) [42] have been proposed to improve the performance on shoreline extraction over anthropized areas or in challenging conditions. Few works suggest that shorelines can be extracted also from S1 with an accuracy of around 1 pixel, such as in [43] where shorelines from an intertidal area were extracted with an accuracy of around 1 pixel (13 m) (Mean Absolute Error).

The aim of this paper is to create a robust and repeatable methodology to extract the "instantaneous shoreline" that can work both for optical and SAR images. The open, easy-to-use and free-of-charge satellite images, namely, the Sentinel products, of two Mediterranean beaches, are used. An experimental algorithm (used in a previous work of the authors [44]) is tested and compared with two algorithms. The shorelines extracted from the S2 and S1 images are validated, at first, with GNSS (Global Navigation Satellite System) measurements, as it is often done in the literature [45,46]. Subsequently, they are compared with the shorelines extracted from two commonly used methods: Canny Edge Detector and CoastSat tool. The advantage of the proposed approach is the use of the same algorithm (J-Net) for shoreline extraction from S1 and S2, only varying the pre-processing strategy. Moreover, the time lag between satellite-derived shorelines is shorter thanks to the capacity to derive data from two different constellations, even with the presence of clouds. This is a key advantage to provide enhanced monitoring and management of coastal areas.

The paper is organized as follows: in Section 2, the study sites and methods are described, and the new methodology for shoreline extraction is presented. Section 3 illustrates the obtained results. GNSS measurements are used as ground truth to compute the achieved accuracy of the satellite-derived shorelines. The results are then compared

to the Canny Edge Detector and the CoastSat tool. Finally, the discussion is developed in Section 4 and the main conclusions of the work are listed in Section 5.

2. Materials and Methods

2.1. Study Areas

Shoreline extraction is conducted in two sandy beaches in Catalunya, north-western Mediterranean Sea (Figure 1).
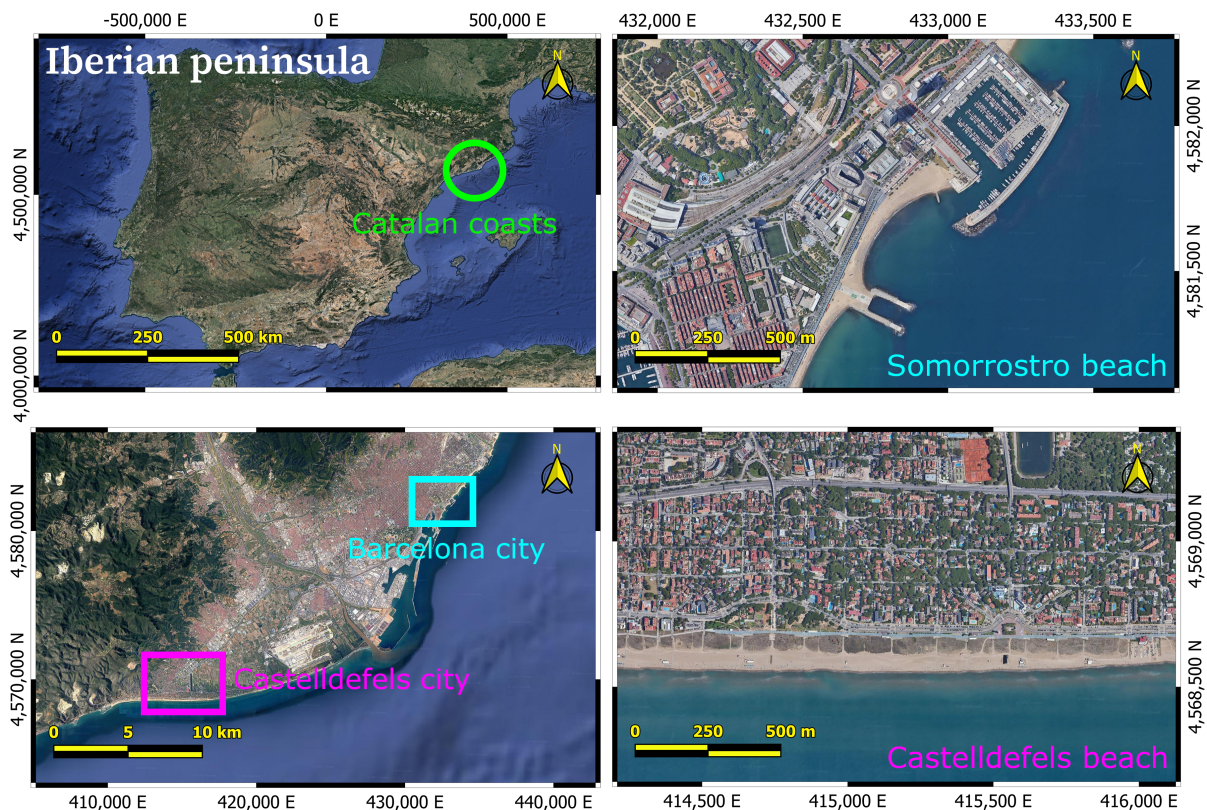

Figure 1. Geographical location of the studied beaches in Castelldefels and Barcelona cities (Spain) Source: Google maps, images from TerraMetrics, CNES/Airbus, Institut Cartogràfic de Catalunya, Landsat/Copernicus, Maxar Technologies.

The beach of Castelldefels is long, flat and wide, with light-brown fine sand that runs for about 5 km along generally shallow and clean waters. It is located 21.2 km away from the city centre of Barcelona, in the south-eastern direction. Somorrostro is, instead, a steeper beach, with a length of about 500 m and surrounded by man-made groins, covered with a mixture of brown fine sand and pebbles. It is located in Barcelona city, between Hospital del Mar and Marina Street in the Ciutat Vella district.

The wave conditions in the central Catalan coast are generally mild, with a significant wave height below 2 m, because the fetch is limited by surrounding landmasses in most directions and winds in the region are generally light to moderate in strength. However, a few storms with significant wave heights from 2 to 5 m can reach the coast every year from the eastern and southern directions, usually concentrated in the autumn and winter seasons. The astronomical tides in the Western Mediterranean Sea feature a small range, of about 20 cm on average, so that inter-annual variability and storm surges, with sea level increments up to 50 cm, can be more significant.

2.2. Sentinel-1 and -2 Imagery and GNSS Data Sets

The Earth Observation (EO) dataset for the present case study is composed of Sentinel-1 and Sentinel-2 images. Sentinel is the mission within the Copernicus programme, an initiative of the European Commission (EC) and the European Space Agency (ESA). The

Copernicus programme is based on observation data received from EO satellites and ground-based information [47,48].

Sentinel-1 is a SAR system, working in C-band (central frequency of 5.404 GHz), and it is made up of 2 satellites, Sentinel-1A and Sentinel-1B, sharing the same orbital plane. With both satellites operating (so until December 2021), the revisit time is 6 days. As it is well known, it operates in four acquisition modes and images are provided in 3 levels. In addition, the acquisition geometry could be ascending or descending, depending of the orbit path, which is, respectively, from north to south and vice versa. In this work, the IW-GRD (Interferometric Wide - Ground Range Detected) level with 10 m resolution is considered, which consists of focused SAR data that have been detected, multi-looked and projected to ground range using an Earth ellipsoid model and contain only the amplitude information. Descending images are selected because of the beaches' geometry. VH polarization is used since the contrast between water and land is more evident.

Sentinel-2 is an optical multispectral system which comprises a constellation of two polar-orbiting satellites (Sentinel-2A and Sentinel-2B), following a sun-synchronous orbit, phased at 180° to each other. The revisit time is 5 days and the sensor can acquire 13 spectral bands in the visible, NIR (Near InfraRed) and SWIR (Short Wave InfraRed) ranges (four bands at 10 m, six bands at 20 m and three bands at 60 m spatial resolution). Sentinel-2 products are available for users in two levels, and in this work, Level-2A is used.

A field campaign of GNSS measurements was carried out in the two studied beaches from May 2017 until March 2018. A total of 10 and 5 shorelines were measured in Castelldefels and Somorrostro, respectively (Table 1), and they were used as ground truth to validate the derived shorelines.

Table 1. GNSS (Global Navigation Satellite System) data acquisition dates, Sentinel-2 (S2) and Sentinel-1 (S2) imagery dates and relative time gaps.

Shoreline GNSS date	S2 imagery date	Time gap S2 (days)	S1 imagery date	Time gap S1 (days)
Castelldefels Beach				
2017/05/31	**2017/06/02**	2	**2017/05/31**	0
2017/11/20	**2017/11/19**	1	**2017/11/21**	1
2017/11/23	**2017/11/19**	4	**2017/11/21**	2
2017/11/27	2017/12/09	12	2017/11/27	0
2017/11/28	2017/12/09	13	2017/11/27	1
2018/01/17	**2018/01/18**	1	**2018/01/20**	3
2018/01/18	**2018/01/18**	0	**2018/01/20**	2
2018/03/14	**2018/03/14**	0	**2018/03/15**	1
2018/03/19	2018/03/14	5	2018/03/21	2
2018/03/21	2018/03/14	7	2018/03/21	0
Somorrostro Beach				
2017/10/06	**2017/10/10**	4	**2017/10/04**	2
2017/11/02	**2017/10/30**	3	**2017/11/03**	1
2017/11/07	**2017/11/09**	2	**2017/11/09**	2
2017/11/13	**2017/11/14**	1	**2017/11/15**	2
2017/11/15	**2017/11/14**	1	**2017/11/15**	0

In bold, the actual dates taken into account for this research. The time gap is the number of days between GNSS and the images' dates.

The GNSS shoreline position was tracked using an Ashtech Pro.Mark2 system from Thales Navigation in the kinematic relative positioning method. This Differential Global Positioning System (dGPS) consists of two receivers that acquire and store the raw satellite data. One receiver, the base, was positioned at the geodesic vertex of the Cartographic and Geological Institute of Catalonia, while the other, after being synchronized for 5 min at another geodesic vertex, was carried in a backpack by a person walking on foot. The people in charge of walking were experienced researchers and they systematically walked in the middle of the swash zone (i.e., by visually detecting the intermediate position between wave runup and rundown). The resolution provided by the dGPS after post-processing the raw data is 1–3 cm for the planimetry and 10 cm for the altimetry, much lower than the spatial resolution of the satellite images. The dates of the reference GNSS measurements are shown in the first column of Table 1, which also shows Sentinel-2 and Sentinel-1 acquisition dates with the time gap between GNSS measurements and satellite images.

As it can be seen, the time gap between Sentinel-2 images and GNSS measurements is, for some days, really high (ranging from 5 to 13 days). This does not happen for Sentinel-1 images. As is known, one of the main disadvantages of optical systems such as Sentinel-2 is that no data are available when there are clouds covering the scene. SAR systems, working in the microwave range of the electromagnetic spectrum, can also acquire data during the night and in any weather conditions. As their measures may not correspond to the same situation of the reference data and the results may be compromised, Sentinel-2 images with a time gap of more than 4 days are discarded from the analysis. Although the final time gaps are short and the hydrodynamic variability in the area is typically mild (Section 2.1), its potential influence on shoreline extraction will be checked (Section 4.1). On the other hand, all Sentinel-1 data, as they are SAR data, can be used, but to maintain consistency with optical data, only the images corresponding to the same GNSS dates are considered. The dates taken into account for this research are highlighted in bold in Table 1. The Sentinel-1 dataset consists of seven images before and seven after the days of interest, in order to apply the multi-temporal speckle filtering used to reduce the speckle effects.

In Figure 2, as examples, a crop of two original images in Castelldefels (Sentinel-2 taken on 2018/01/18 and Sentinel-1 taken on 2018/01/20) are shown. The reference system is WGS84/UTM, Zone 31 N (EPSG: 32631).
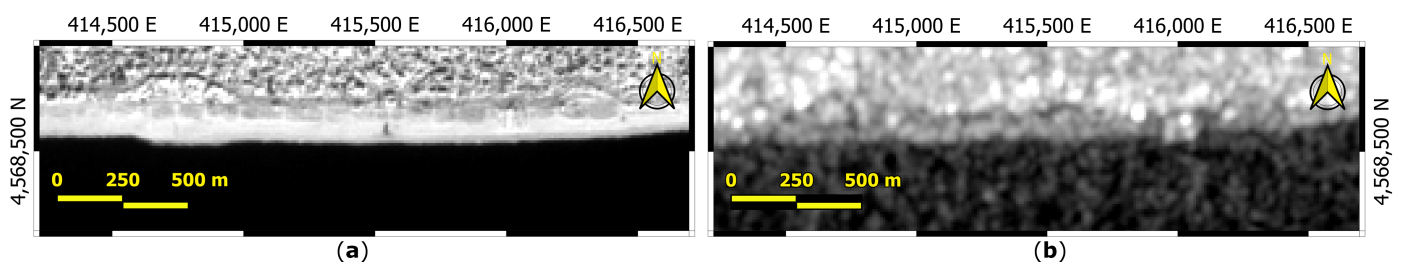

Figure 2. Crops of (**a**) the original S2 NIR (Near InfraRed) band and (**b**) S1 VH polarization images.

2.3. Pre-Processing of S1 and S2 Images

In order to remove geometric and radiometric distortion (and speckle filtering in the case of SAR images), pre-processing is performed on both Sentinel-1 and Sentinel-2 images.

Sentinel-1 images pre-processing is a key issue of SAR elaboration because, for a better identification of the shoreline, it is essential to reduce noise while preserving the edges. A crucial step is the reduction of the speckle, caused by random constructive and destructive interference resulting in salt and pepper noise throughout the image. The performed pre-processing steps are: thermal noise removal, applying orbit file, calibration, coregistration, multitemporal de-speckle, range doppler terrain correction. Thermal noise removal is applied to remove an additive background energy that causes noise floor, especially in the cross-polarization channel. Then, orbit file is applied, which provides an accurate satellite position and velocity information. During the calibration, pixel values are directly connected to the radar backscatter and coregistration aligns all the slaves with the master

image, creating a unique stack. Then, multitemporal de-speckle is applied to reduce speckle effects. Speckle filtering is still an important issue to be overcome, although there are several approaches and algorithms that have been implemented [49–52]. In this case, the Lee filter with 3×3 window size is used because it is a good compromise between keeping the spatial resolution and preserving the edges. Finally, terrain correction allows compensating topographical distortions.

Sentinel-2 pre-processing, since they are already orthorectified and atmospherically corrected using Sen2Cor processor (SNAP (Sentinel Application Platform) tool) and PlanetDEM Digital Elevation Model (DEM), consists of resampling the bands with spatial resolution from 20 m to 10 m and performing several tests in order to find the best band and indices to detect the shoreline. Resampling to 10 m is performed on 11 (SWIR) and 12 (SWIR) bands. Bands with spatial resolution of 60 m are not considered due to their not-optimal resampling. Bands and indices tested as input for the new algorithm were NIR, SWIR, NDVI (Normalized Difference Vegetation Index), NDWI (Normalized Difference Water Index) and SAVI (Soil Adjusted Vegetation Index) (Figure 3). NIR and SWIR are, respectively, band number 8 and 12. The other three are combination of bands (Equations (1)–(3)).
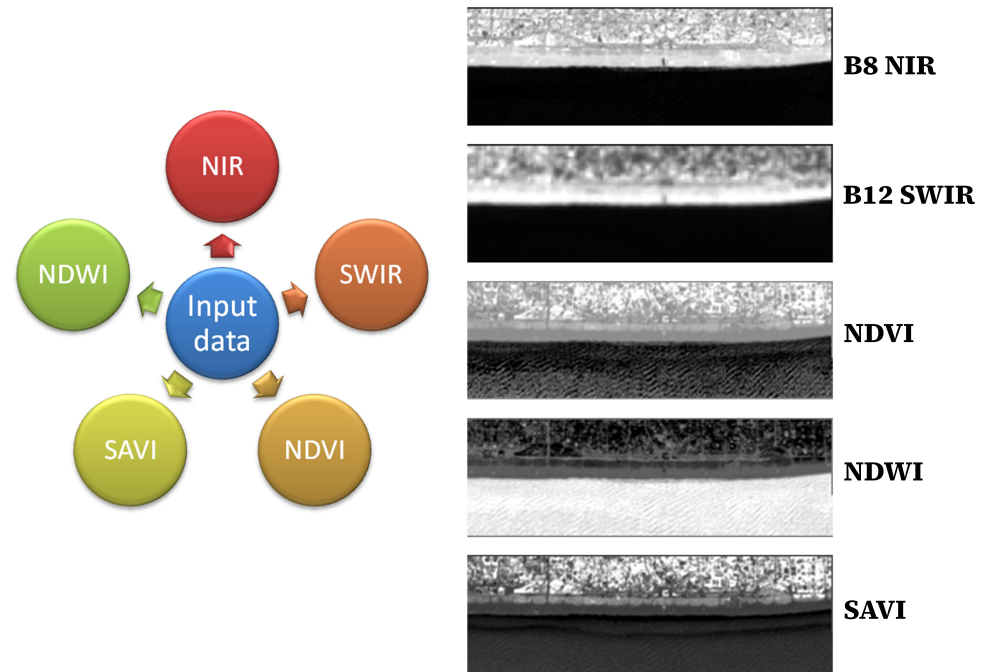

Figure 3. Sentinel-2 tested bands and indices for shoreline detection.

$$NDVI = \frac{NIR - RED}{NIR + RED} \tag{1}$$

$$NDWI = \frac{BLUE - NIR}{BLUE + NIR} \tag{2}$$

$$SAVI = (1 + L) \times \frac{NIR - RED}{NIR + RED + L} \tag{3}$$

SAVI is generally used, as the NDVI, to detect vegetated areas but it is more specific in areas where vegetative cover is low (<40%). The parameter "L" in Equation (3) is a correction factor which ranges from 0 to 1 and it is usually found by trial and error. In this case, a value of 0.5 is used.

As it can be seen from the images in Figure 3 (which are only from Castelldefels but the same applies to Somorrosto beach), the best band for this research turns out to be the NIR (band 8), which visually defined more clearly the separation line between land and water. The NIR band is indeed suitable for discriminating water from wet and dry sand, as it is almost completely absorbed by the water and possible perturbations are minimised by the shallow bottoms [19]. The SWIR band appears more blurry because of the resampling from 20 m to 10 m, while NDVI, SAVI and NDWI show disturbances on the water, produced by waves, or double lines near the shore.

2.4. New Methodology for Shoreline Extraction

The semi-automatic methodology proposed for shoreline extraction takes into account the J-Net Dynamic algorithm, developed by Professor Paolo Massimo Buscema, Director of the Semeion Research Centre of Science of Communication of Rome. The patent concerns Active Connections Matrix Systems (ACM), according to which each image is considered as an active matrix (network) of connected elements (pixels) that develops over time. The main idea upon which this theory is based states that each digital image stores the maximum amount of information within the pixel values and their relationships. Furthermore, it is possible to obtain important information by analysing the reciprocal positions occupied by pixels, as well as their weights. Among all the ACM Systems, J-Net Dynamic is an algorithm working as an edge detector, so it is able to extract the boundaries of the images in an iterative way. A range of values in the equation parameters can be established and the image that better enhances the boundaries between water and land can be chosen. The ACM Systems come from the machine learning and data science community and were originally applied in the medical field. In this paper, their applicability in shoreline monitoring is tested by comparing the results to GNSS measurements. For a complete presentation of ACM algorithms, and, more specifically, of the J-Net Dynamic, see [53–55].

The proposed methodology can be grouped into 4 main blocks: image pre-processing and cropping of the area of interest; shoreline extraction using J-Net Dynamic algorithm; geoprocessing and finally validation and comparisons. The detailed methodology is shown in Figure 4. The first step consists of creating a crop of the image in the area of interest (Figure 4a). Second, the experimental algorithm, J-Net Dynamic, is applied (Figure 4b), which keeps 3 pixels in each column following the edge. The black one is the most probable border. Third, pixels with the same value (the black ones) are masked out (Figure 4c), obtaining a binary image which is subsequently converted from raster to vector (Figure 4d), and then from vector to line (Figure 4(e1)). The created lines are, actually, polygons around the pixels and not a continuous line. For this reason, the central points (centroids) of these polygons are extracted (Figure 4(e2)) and, consequently, the points are joined to form a continuous line (Figure 4f). Finally, the shortest distance between the line and by the GNSS measured points is calculated (Figure 4g) for every considered day. Mean and standard deviation (in absolute values) of all the points of each shoreline are determined. Every image in Figure 4 is zoomed in order to better appreciate the differences between the different steps. The procedure is first applied to Sentinel-2 images. Then, Sentinel-1 images are coregistered to the Sentinel-2 ones and the procedure is repeated for SAR images for both test sites. All these steps are performed using QGIS (Quantum Geographic Information System).
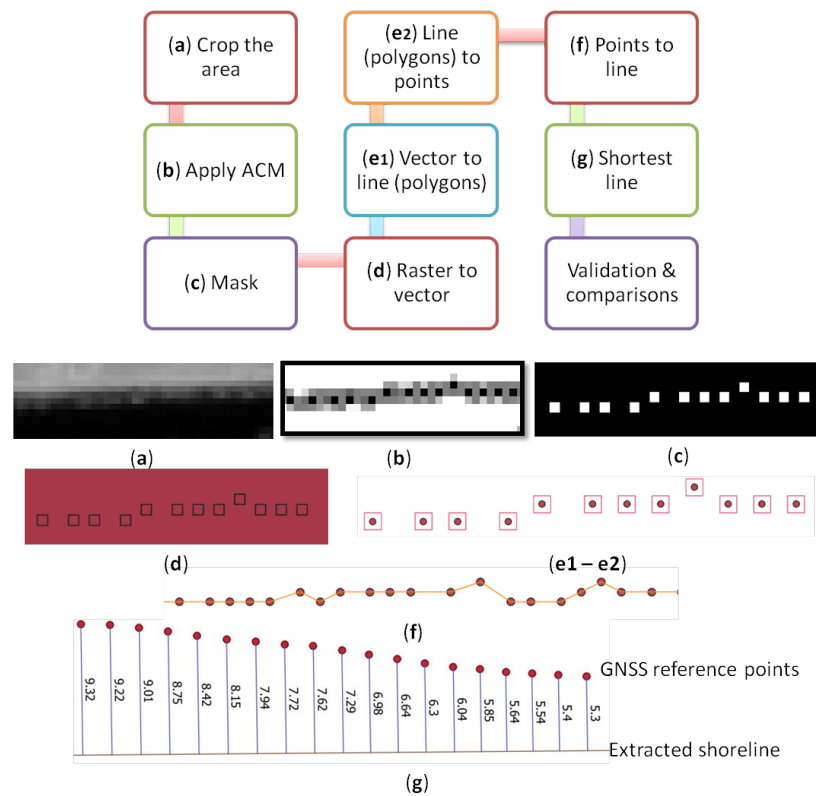
Figure 4. Semi-automatic methodology for shoreline extraction: (**a**) crop of the original NIR band image; (**b**) J-Net Dynamic application; (**c**) mask of pixels with the same value; (**d**) transformation from raster to vector and (**e1**) from vector to line, which are polygons around every pixel, and (**e2**) from line (polygons) to points; (**f**) interpolation to create the final shoreline; (**g**) computation of the shortest distance between extracted line and GNSS measurements (the measures are expressed in metres). The shown example is for a Sentinel-2 image.

2.5. Alternative Detection Methods

In order to compare the performance of the proposed approach with the state-of-the-art tools, both Canny algorithm and CoastSat tool are also used for extracting shorelines from S1 and S2 imagery.

The Canny Edge Detector is an edge detection operator that uses a multi-stage algorithm to detect a wide range of edges in images [56]. The Canny algorithm [57] is composed of 5 steps—noise reduction, gradient calculation, non-maximum suppression, double thresholding and edge tracking by hysteresis.

CoastSat [34,40,58,59] is an open-source, widely used software that enables users to obtain time-series of shoreline position at any coastline worldwide from 30+ years (and growing) of publicly available satellite imagery [34]. It takes advantage of Google Earth Engine (GEE) to retrieve Sentinel-2 images cropped by the user in the area of interest. The images are pre-processed by cloud masking, pansharpening and down-sampling before applying the shoreline extraction algorithm. This algorithm relies on a MNDWI (Modified Normalized Difference Water Index) image obtained using the short-wave infrared band (SWIR) and green band, and a classification of the pixels of the area of interest with a different label (water, white water, sand, and others) based on supervised learning technique. Then, a sand/water threshold is computed automatically using Otsu's thresholding but considering only the pixels labelled as water and sand during the classification step. After the application of the threshold, the shoreline is extracted at sub-pixel level using a marching squares method. In this work, two shorelines from CoastSat were extracted for each date, one using an automatic threshold (with default settings) and the other adjusting manually a threshold (Table 2). In order to compare the experimental algorithm with CoastSat, the MNDWI is also applied in Sentinel-2 images before the ACM.

Table 2. MNDWI (Modified Normalized Difference Water Index) automatic and manual thresholds used to extract shorelines from CoastSat in Castelldefels and in Somorrostro beaches.

Sentinel-2/CoastSat Thresholds			
Image	*GNSS Reference*	*MNDWI auto threshold*	*MNDWI manual threshold*
Castelldefels Beach			
2017/06/02	2017/05/31	−0.2363	−0.0510
2017/11/19	2017/11/20	−0.3117	−0.0930
2017/11/19	2017/11/23	−0.3117	−0.0930
2018/01/18	2018/01/17	−0.2690	−0.0900
2018/01/18	2018/01/18	−0.2690	−0.0900
Somorrostro Beach			
2017/10/10	2017/10/06	−0.2316	0.0130
2017/10/30	2017/11/02	−0.1595	0.0476
2017/11/09	2017/11/07	−0.2823	0.0620
2017/11/14	2017/11/13	−0.2598	0.0321
2017/11/14	2017/11/15	−0.2598	0.0321

3. Results

3.1. Results of the New Methodology

The results of the J-Net Dynamic algorithm compared to the GNSS points are reported in Table 3 for Sentinel-2 and Table 4 for Sentinel-1. Mean and standard deviation are lower in Sentinel-2 images, i.e., shorelines extracted from optical images are closer to reference data, as expected. SAR images are affected by speckle, which worsens significantly the quality of the original image (Figure 2b).

Table 3. Mean and standard deviation of the distances between Sentinel-2 shorelines and GNSS reference points in Castelldefels and in Somorrostro beaches by using the experimental J-Net Dynamic algorithm.

Sentinel-2/J-Net Dynamic			
Image	*GNSS Reference*	*Mean (m)*	*Standard deviation (m)*
Castelldefels Beach			
2017/06/02	2017/05/31	9.0	3.2
2017/11/19	2017/11/20	6.3	4.8
2017/11/19	2017/11/23	6.0	4.7
2018/01/18	2018/01/17	3.3	2.1
2018/01/18	2018/01/18	3.0	2.4
2018/03/14	2018/03/14	2.1	1.8
Somorrostro Beach			
2017/10/10	2017/10/06	4.4	2.9
2017/10/30	2017/11/02	2.5	3.3
2017/11/09	2017/11/07	4.6	2.9
2017/11/14	2017/11/13	4.0	3.4
2017/11/14	2017/11/15	4.7	4.0

Table 4. Mean and standard deviation of the distances between Sentinel-1 shorelines and GNSS reference points in Castelldefels and in Somorrostro beaches by using the experimental J-Net Dynamic algorithm.

Sentinel-1/J-Net Dynamic			
Image	*GNSS Reference*	*Mean (m)*	*Standard deviation (m)*
Castelldefels Beach			
2017/05/31	2017/05/31	21.0	13.0
2017/11/21	2017/11/20	10.5	6.4
2017/11/21	2017/11/23	10.6	6.9
2018/01/20	2018/01/17	9.3	5.8
2018/01/20	2018/01/18	9.9	6.3
2018/03/15	2018/03/14	15.9	7.9
Somorrostro Beach			
2017/10/04	2017/10/06	31.2	22.3
2017/11/03	2017/11/02	35.9	20.5
2017/11/09	2017/11/07	29.9	18.0
2017/11/15	2017/11/13	32.7	19.9
2017/11/15	2017/11/15	31.1	20.0

Referring to Castelldefels and considering Sentinel-2 images, extracted shorelines accuracy is sub-pixel, with a minimum of 2.1 m and a maximum value of 9.0 m. Despite speckle effects, accuracy achieved by Sentinel-1 shorelines ranges from 9.3 to 21 m. Images compared with more than one GNSS reference data point have similar mean values. This can be seen in Sentinel-2 images of 2017/11/19 and 2018/01/18 and Sentinel-1 images 2017/11/21 and 2018/01/20, which were compared to two GNSS surveys, obtaining very similar results. In both optical and radar images, the obtained accuracy ranged from sub-pixel to 2 pixels in Castelldefels beach.

Regarding Somorrostro Sentinel-2 images, the extracted shoreline accuracy is sub-pixel, with a minimum of 2.5 m and a maximum value of 4.7 m. The results confirm the trend obtained in Castelldefels. The biggest difference occurs in the SAR dataset. The achieved accuracy is around 3 pixels for all the images, with a minimum of 29.9 m and a maximum value of 35.9 m.

3.2. Comparison with Canny Algorithm

The obtained results, shown in Tables 5 and 6, are compared with techniques currently used in the literature, starting with the Canny Edge Detector, explained in Section 2.5.

In Castelldefels beach, the extraction is possible but, generally, the obtained shorelines are similar or worse (depending on the day) from the ground truth (GNSS measurements) than J-Net Dynamic. Canny Edge Detector, indeed, proves to be powerful on optical images using NIR band, achieving minimum mean value of 3.2 m, sub-pixel accuracy and maximum mean value of 12.7 m. Again, the accuracy attained by this detector in SAR images is lower due to the speckle effect, with minimum mean value of 7.5 m and maximum of 25.4 m. In both cases, the mean distance values of the same image compared to different GNSS measurements are similar, as was the case with the J-Net Dynamic algorithm. The results are therefore quite similar in the two algorithms, the achieved accuracy being from sub-pixel to 1 pixel (10 m) in Sentinel-2 and 1-2 pixels (10–20 m) in Sentinel-1 imagery. In Sentinel-2, half of the mean values are closer to reference data by applying J-Net Dynamic and the other half—by applying Canny. In SAR images, the experimental algorithm (J-Net Dynamic) detects the shoreline closer to GNSS references than the common one (Canny) in four out of six cases. This proves that J-Net Dynamic is less sensitive to speckle and to artefacts present in the image.

Table 5. Mean and standard deviation of the distances between Sentinel-2 shorelines and GNSS reference points in Castelldefels and in Somorrostro beaches by using the commonly used Canny Edge Detector algorithm.

Sentinel-2/Canny			
Image	*GNSS Reference*	*Mean (m)*	*Standard deviation (m)*
Castelldefels Beach			
2017/06/02	2017/05/31	3.2	2.6
2017/11/19	2017/11/20	5.2	3.1
2017/11/19	2017/11/23	5.3	3.2
2018/01/18	2018/01/17	12.7	2.9
2018/01/18	2018/01/18	10.3	3.1
2018/03/14	2018/03/14	10.6	2.8
Somorrostro Beach			
2017/10/10	2017/10/06	5.2	2.6
2017/10/30	2017/11/02	-	-
2017/11/09	2017/11/07	12.6	4.9
2017/11/14	2017/11/13	12.2	5.4
2017/11/14	2017/11/15	14.1	5.9

Table 6. Mean and standard deviation of the distances between Sentinel-1 shorelines and GNSS reference points in Castelldefels and in Somorrostro beaches by using the commonly used Canny Edge Detection algorithm.

Sentinel-1/Canny			
Image	*GNSS Reference*	*Mean (m)*	*Standard deviation (m)*
Castelldefels Beach			
2017/05/31	2017/05/31	24.4	9.9
2017/11/21	2017/11/20	7.5	5.0
2017/11/21	2017/11/23	8.2	5.9
2018/01/20	2018/01/17	25.4	9.6
2018/01/20	2018/01/18	24.3	10.6
2018/03/15	2018/03/14	24.0	12.1
Somorrostro Beach			
2017/10/04	2017/10/06	-	-
2017/11/03	2017/11/02	-	-
2017/11/09	2017/11/07	-	-
2017/11/15	2017/11/13	-	-
2017/11/15	2017/11/15	-	-

Regarding Somorrostro, the border between water and land is not well defined by the Canny Detector, especially for SAR images. In the optical ones, the algorithm does not work in one day and it provides shorelines significantly further from the reference compared to J-Net Dynamic. Indeed, the minimum "Canny value" is 5.2 m, while the maximum is 14.1 m. In SAR images, the Canny algorithm cannot provide any results, proving to be more sensitive to speckle effects. It is not capable of extracting the shoreline where a higher noise level is present due to the scatterers founded in the image (Figure 5). The edges are not well extracted throughout all SAR images, the shorelines are interrupted in correspondence with the higher scattering from the port. It seems that the commonly used Canny algorithm is not able to extract the shoreline on SAR images when the beach is steep and narrow and is surrounded by ports or other man-made artefacts. The comparison between J-Net Dynamic and Canny results in Sentinel-2 and -1 images is reported in graphical format in Appendix A, Figures A1 and A2, respectively considering Castelldefels beach and in Figures A3 and A4 in Somorrostro beach.
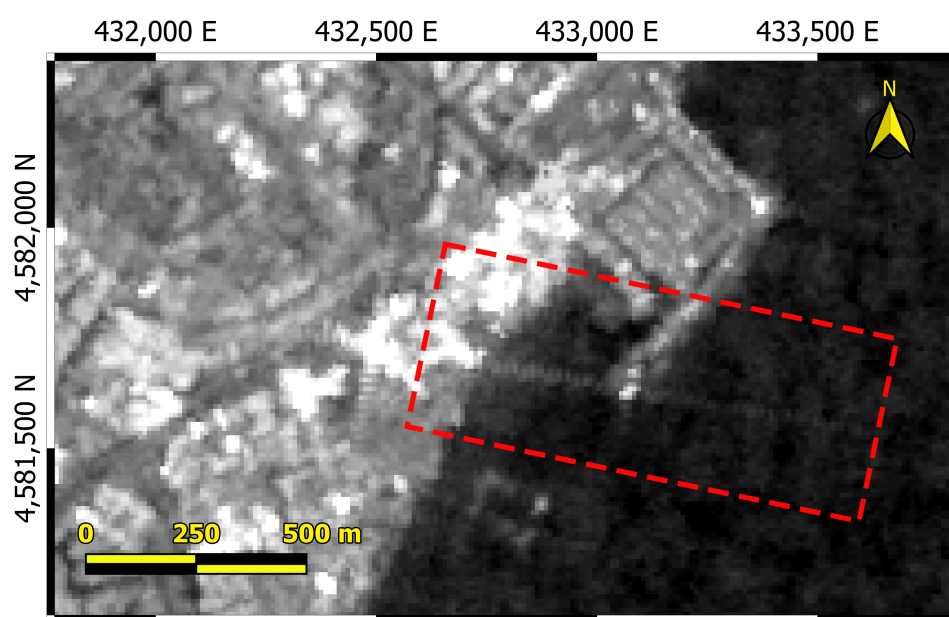

Figure 5. Zoom of Somorrostro Sentinel-1 SAR image. The red rectangle points at the scatterers that create sidelobes, which introduce noise for shoreline extraction.

3.3. Comparison with CoastSat Tool

A further comparison is performed with the shorelines extracted from CoastSat. As mentioned above, automatic and manual thresholds are used as reported in Table 2, while the results are provided in Table 7.

Generally, in both beaches, the CoastSat with manual threshold provides shoreline closer to the GNSS points than those of the automatic thresholds, as expected. Moreover, during the day 2018/03/14, the area is slightly covered by fog and CoastSat cannot extract the shoreline. The accuracy is sub-pixel, reaching a lower value of 1.7 m in Castelldefels and 3.6 m in Somorrostro, compared, respectively, to 5.4 m and 5.3 m for the automatic threshold. In addition, in Somorrostro, the obtained distances are greater than in Castelldefels. The extraction seems to be more reliable in the flat and wide beach than in the steeper one.

As it can be seen from the results in Table 8, the distances obtained by the application of MNDWI + J-Net Dynamic are generally lower than the ones extracted from MNDWI automatic threshold of CoastSat, but higher than the ones with the manual threshold. The minimum value achieved by MNDWI + J-Net Dynamic is 3.4 m in Castelldefels and 5.1 m in Somorrostro, while the higher values are 13.2 m and 16.6 m, respectively. As previously noticed, also in this case, the distances for the wide and large beach of Castelldefels are lower than Somorrostro.

Table 7. Mean and standard deviation of the distances between Sentinel-2 shorelines and GNSS reference points in Castelldefels and in Somorrostro beaches by using CoastSat with both automatic and manual thresholds.

Sentinel-2/CoastSat					
Image	*GNSS Reference*	*Mean (m)*	*St. Dev. (m)*	*Mean (m)*	*St. Dev. (m)*
		Auto Threshold		*Manual Threshold*	
Castelldefels Beach					
2017/06/02	2017/05/31	10.9	2.4	3.0	1.6
2017/11/19	2017/11/20	15.5	1.3	4.6	2.0
2017/11/19	2017/11/23	15.6	1.1	4.7	1.9
2018/01/18	2018/01/17	7.6	1.7	2.0	1.1
2018/01/18	2018/01/18	5.4	1.8	1.7	1.0
Somorrostro Beach					
2017/10/10	2017/10/06	15.9	3.1	6.8	3.6
2017/10/30	2017/11/02	20.8	14.0	9.2	7.8
2017/11/09	2017/11/07	19.7	4.5	3.6	3.3
2017/11/14	2017/11/13	5.5	4.3	10.3	3.9
2017/11/14	2017/11/15	5.3	5.2	8.6	3.8

Table 8. Mean and standard deviation of the distances between Sentinel-2 shorelines and GNSS reference points in Castelldefels and in Somorrostro beaches by using at first the MNDWI and then the experimental J-Net Dynamic algorithm.

Sentinel-2/MNDWI Plus J-Net Dynamic			
Image	*GNSS Reference*	*Mean (m)*	*Standard deviation (m)*
Castelldefels Beach			
2017/06/02	2017/05/31	2.7	2.3
2017/11/19	2017/11/20	13.2	3.6
2017/11/19	2017/11/23	13.0	3.8
2018/01/18	2018/01/17	3.4	2.2
2018/01/18	2018/01/18	4.3	2.9
Somorrostro Beach			
2017/10/10	2017/10/06	14.6	4.5
2017/10/30	2017/11/02	13.0	11.0
2017/11/09	2017/11/07	16.6	7.3
2017/11/14	2017/11/13	5.8	3.5
2017/11/14	2017/11/15	5.1	3.4

The comparison between J-Net and CoastSat results is shown in Appendix A, Figure A5 considering Castelldefels beach and Figure A6 for Somorrostro beach.

4. Discussion

4.1. Role of the Oceanographic Conditions on the Obtained Errors

Beach shorelines are very dynamic, responding to wave and sea level conditions. During storms, which can last 1–2 days in the Mediterranean Sea, the shoreline typically moves onshore because of the beach inundation produced by the sea level increase and wave run-up due to wave breaking and/or storm surge. This temporal shoreline recession can be of tens of meters in tideless beaches such as the studied ones [60], depending mainly on the intensity of the storm and the beach slope. After the storm, when the sea level returns to its mean position, the shoreline moves again seaward. However, storms can also produce offshore sediment transport so a certain "permanent" shoreline recession can be often observed after them. The amount is variable but always smaller than the temporal recession due to inundation. Some authors [60,61] have shown maximum changes of the order of 10 m in Somorrostro and Castelldefels, respectively, during large storms. In the periods without storms (lasting from weeks to months), sediment transport is typically onshore-directed and the shoreline can slowly accrete.

As aforementioned, the established time gap between the satellite images and GNSS measurements is up to 4 days (Table 1). It is important to check what part of the obtained differences between satellite and GNSS shorelines could be due to a real change in shoreline position, either due to variations in wave and sea level conditions during the different dates or due to storm erosion that may have occurred between the two dates. To check this in the case of Castelldefels beach, the dataset developed by De Swart et al. [61], which covered the study period of the present contribution, is used. The daily shoreline positions extracted from video images are analysed, together with the wave conditions from a buoy located at 68 m depth and propagated using the SWAN (Simulating WAves Nearshore) model to 10 m depth in front of the beach. No daily video-derived shorelines are available for Somorrostro during the study period, but the wave conditions at 10 m depth in front of the beach are computed using optical approximation and wave energy conservation. In both sites, sea level conditions measured inside Barcelona harbour are also considered.

In Table 9, the oceanographic conditions during the studied dates are listed. Specifically, Δz_s and ΔH_s contain the difference between the two dates in the Barcelona harbour sea surface level and in the significant wave height at 10 m depth in front of each beach, respectively. Moreover, E_{acc} is a proxy of the wave energy at deep water accumulated during the time gap, which can be an indicator of potential storm-induced shoreline changes [62], and Δx_s is the difference between the two dates in the alongshore-averaged videoed shoreline position, available only in the case of Castelldefels. The variability in the Barcelona harbour sea surface is small (<0.15 m) in all the studied dates and no significant effects are to be expected in terms of shoreline motion. In most of the studied dates for GNSS and satellite images in Castelldefels beach, there are calm wave conditions (significant wave height, $H_s < 0.50$ m). In particular, in all the optical images of Castelldefels and the first two day of SAR images, the H_s values were similar (differences < 0.15 m) both in GNSS and in the satellite images dates, and no storms occurred during the time gap (Table 9).

Accordingly, the video-derived shorelines in that beach show movements smaller than 1–2 m, so in the range of the video-extraction method accuracy [17] and significantly lower than the spatial resolution of the satellite images. In the last four days of SAR images in Castelldefels, and especially those in January and March 2018, there are larger H_s, of 0.70 m to 0.90 m, either during the GNSS surveys or during the S1 images. Due to the time gaps, H_s differences of up to 0.60 m occur between the pairs of dates and, accordingly, more significant shoreline motions between 3 and 8 m can be detected from video images (Table 9). Thus, although there could be real changes in shoreline position, they are not detectable on Sentinel images. The higher value of variation is lower than the spatial resolution of the images.

Table 9. Oceanographic conditions during the studied shoreline dates (of the satellite images and of the GNSS surveys).

Image Date	GNSS Date	Gap (d)	Δz_s (m)	ΔH_s (m)	E_{acc} (m²h)	Δx_s (m)
		Castelldefels Beach S2				
2017/06/02	2017/05/31	2.1	0.05	0.05	8.1	−0.2
2017/11/19	2017/11/20	1	−0.01	0.01	5	0.4
2017/11/19	2017/11/23	4.2	0.01	0.15	12.4	−1.8
2018/01/18	2018/01/17	0.8	−0.03	0.09	22.1	0
2018/01/18	2018/01/18	0.1	0.02	0.13	1.9	0
2018/03/14	2018/03/14	0.1	0.05	0	0.5	0
		Castelldefels Beach S1				
2017/05/31	2017/05/31	0.1	−0.03	−0.02	1.3	0
2017/11/21	2017/11/20	1	−0.03	0.04	3.5	−0.4
2017/11/21	2017/11/23	2.2	−0.01	0.18	4.2	−2.6
2018/01/20	2018/01/17	2.8	−0.09	0.45	31.5	−7.6
2018/01/20	2018/01/18	2.1	−0.04	0.49	11.4	−5.5
2018/03/15	2018/03/14	1.1	−0.09	−0.6	15.7	4.4
		Somorrostro Beach S2				
2017/10/10	2017/10/06	4.1	−0.15	0.2	60.9	-
2017/10/30	2017/11/02	2.9	0.05	0.02	39.4	-
2017/11/09	2017/11/07	2.1	0.06	0.24	42	-
2017/11/14	2017/11/13	1.1	−0.15	−0.14	36.4	-
2017/11/14	2017/11/15	1.1	0.02	−0.31	54.1	-
		Somorrostro Beach S1				
2017/10/04	2017/10/06	1.9	0.09	−0.1	13.5	-
2017/11/03	2017/11/02	1.1	0	0.28	4.8	-
2017/11/09	2017/11/07	2.1	0.06	0.24	42	-
2017/11/15	2017/11/13	2.1	−0.15	0.07	85.3	-
2017/11/15	2017/11/15	0.1	−0.02	0.09	4.4	-

In the Barcelona cases, there are higher energetic waves (H_s up to 1.2 m) during dates, with accumulated storm energy between pairs of dates from 30 to 80 m²h in many of the dates (corresponding to a Class 1 storm in [62]) and changes in H_s between GNSS survey and image dates ranged from 0.20 m to 0.30 m. However, given that the beach slope in Somorrostro is higher than in Castelldefels, the effect of these changes in the shoreline position might be small and, in any case, lower than the spatial resolution of the images.

Thereby, the differences occurring in the present contribution between satellite-derived and GNSS shorelines are not related to changes in oceanographic conditions. The larger standard deviations obtained in both sites using S1 images are due to the level of noise present in radar images, mainly caused by speckle and man-made structures.

4.2. Analysis of the Obtained Results

The obtained results generally show that the semi-automatic methodology for shoreline extraction using the experimental algorithm J-Net Dynamic provides good accuracy. An example of the shorelines extracted with each method is reported in Figure 6.
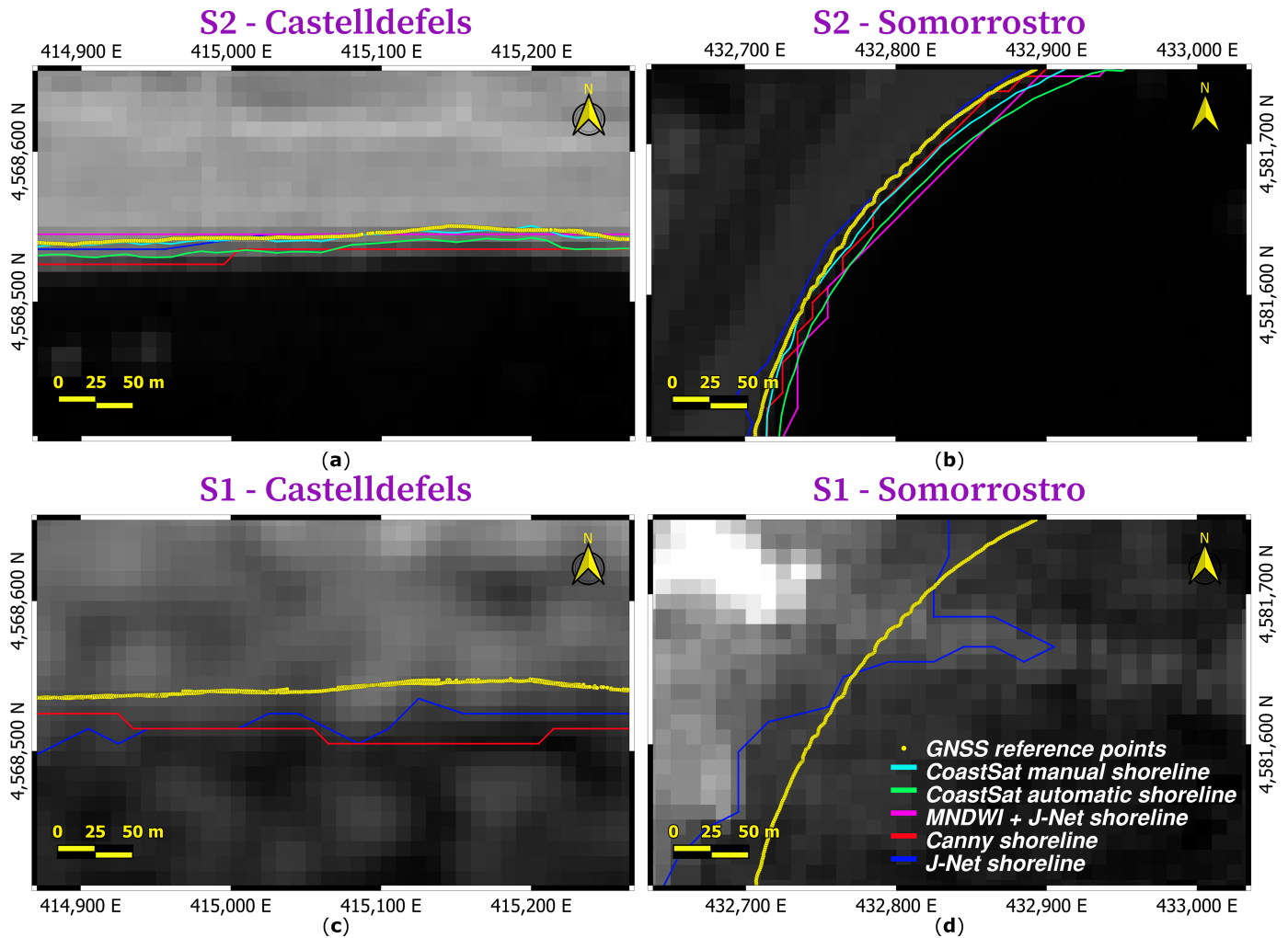

Figure 6. All extracted shorelines: (**a**) S2 Castelldefels, date 2017/06/02, (**b**) S2 Somorrostro, date 2017/10/10; (**c**) S1 Castelldefels 2017/05/31; (**d**) Somorrostro, dates 2017/10/04. GNSS reference points (yellow); CoastSat shoreline extracted with manual (light blue) and automatic (red) thresholds; shoreline extracted by J-Net Dynamic over the MNDWI image (pink); Canny-derived shoreline (red); J-Net Dynamic extracted shoreline (blue).

In the validation with GNSS measurements, the mean distances reach sub-pixel values for optical (Table 3) and one pixel for SAR images (Table 4) in the wide and flat coast of Castelldefels. In the steeper and narrow Somorrosto beach, it reaches sub-pixel accuracy for Sentinel-2 images (Table 3) but 3 pixel for SAR (Table 4). Generally, the accuracy is better in optical than in SAR imagery and in Somorrostro it is worst than in Castelldefels. The main sources of noise are the speckle effect and the man-made artifacts, but the geological differences between two beaches might play a role. Somorrostro beach is steeper than the Castelldefels one and its width is smaller. Looking at Figure 5, the noise reflection from specific scatterers along the port is clearly visible and it creates a little segment which affects the image and the shoreline detection algorithm.

The Canny Edge Detector cannot extract the shorelines in SAR imagery. Not only is it more sensible to speckle compared with J-Net, but it also presents more difficulty when the beach is surrounded by man-made structures and the level of noise increases. The

mean and standard deviation on optical images are comparable, while on SAR, the J-Net provided shorelines closer to the ground truth (Tables 5 and 6).

Using CoastSat, the results in Somorrostro beach reach one-pixel accuracy, decreasing to sub-pixel in Castelldefels (Table 7). The manual threshold detects the closest shoreline, but the automatic one extracts more distant shorelines compared with J-Net. In addition, J-Net Dynamic can be applied also on SAR images, which cannot be done with CoastSat. In one case, CoastSat is not able to extract the shoreline due to the presence of haze. In the last two days, there is also an inversion of the values trend probably due to the presence of clouds. The automatic threshold tends to overestimate the value and in cloud conditions, it works better than the manual threshold due to the incorrect human interpretation.

Finally, general considerations can be extrapolated from the results. First, when the beach is flat and wide without hard structures nearby, the extraction is more reliable and closer to the ground truth, especially in SAR imagery. This is in agreement with other studies, where it was found that the extracted shoreline needed manual corrections in urban and port areas. Second, the applicability of radar satellite imagery for shoreline extraction is possible in flat and wide beaches, but, the accuracy is lower than in optical images, with errors of 1–2 pixels instead of sub-pixel optical accuracy. However, since optical images cannot give any information during the night or bad weather, under this conditions, SAR images can be a good complement. Moreover, one of the greater advantage of SAR images is the high capacity for water distinction. Therefore, this kind of sensor can be used as an additional information source for monitoring, both in terms of water body identification and in shoreline studies.

5. Conclusions

In this work, a successful semi-automatic procedure to extract the shoreline is found. The satellite dataset consists of optical Sentinel-2 and SAR Sentinel-1 imagery over two kinds of sandy beaches: the flatter Castelldefels and the steeper Somorrostro (Barcelona). An experimental algorithm, called J-Net Dynamic, is tested and validated against the ground truth, which is constituted by GNSS measurements. Then, another two comparisons with state-of-the-art tools are performed in order to strengthen the methodology. The obtained results are compared with a common algorithm, the Canny Edge Detector and with CoastSat tool, both using automatic and manual thresholds.

The J-Net Dynamic algorithm, deriving from the machine learning world and mainly used for medical purposes, was demonstrated to be powerful also on satellite remote sensed images for coastal applications. Sub-pixel accuracy (<10 m) is reached in optical images and errors increase to 1–2 pixels in SAR images.

Considering Canny, the results are more or less comparable in the optical images but J-Net shows better performance with SAR imagery. It appears to be less sensitive to the speckle effect and man-made structures close to the beach. The comparison with the shorelines extracted from optical images using CoastSat software shows that the experimental algorithm provides an extraction closer to the reference than the one obtained by using the automatic thresholds in CoastSat, but further in case of the manual one.

Copernicus Sentinel-1 and -2 high-resolution images are full, open, free of charge, easy to download and to use, therefore, they are important data sources for continuous monitoring. The present research demonstrates that a sub-pixel accuracy can be reached, which makes them appropriate tools to support management and planning by monitoring the position of the shoreline and, as a consequence, erosion and accretion in the coastal areas. The present results and analysis lead to recommendations and best practices useful for the scientific community for shoreline studies. They can be summarized as follows: especially when using SAR images, it is suggested not to use Canny but J-Net Dynamic algorithm; shoreline extraction using SAR images in urban beaches can be problematic due to the noise created by nearby solid structures; in optical images, it is recommended to use CoastSat with manual threshold or, alternatively, J-Net Dynamic rather than CoastSat with

automatic threshold; when possible, Sentinel-1 and -2 free-of-charge images can be used for shoreline extraction with one-pixel and sub-pixel accuracy, respectively.

A future study could, at first, implement the semi-automatic procedure in a software, in order to allow a quick extraction of the shoreline. Storing a database of shoreline over time allows to perform a time-series analysis and, consequently, provide a possible intervention plan. In addition, the influence of the ascending and descending SAR imagery for the shoreline extraction may be studied in detail. Moreover, the proposed approach should be extended to additional sandy beaches, to further confirm the influence of the beach slope and anthropic artefacts in the extraction of the shoreline from S1 imagery. This methodology could also be tested on rocky beaches, both with and without man-made structures. Further work should include an integration and/or a fusion of both sensors to enhance the monitoring of shorelines before, during and after storms or to derive linear regression rates of shoreline displacement using combined shorelines. Finally, Very High Resolution (VHR) satellite images, such as optical WorldView-2 and SAR COSMO-SkyMed, could also be tested.

Author Contributions: Conceptualization, S.Z., D.D., M.A. and M.C.-G.; methodology, S.Z., D.D., M.A. and M.C.-G.; validation, S.Z., M.C.-G., E.A., F.R. and G.S.; formal analysis, S.Z., E.A. and F.R.; investigation, S.Z., E.A. and F.R.; resources, S.Z., D.D., M.A., M.C.-G., E.A., F.R. and G.S.; writing—original draft preparation, S.Z.; writing—review and editing, S.Z., D.D., M.A., M.C.-G., E.A., F.R. and G.S.; visualization, S.Z., D.D., M.A., M.C.-G., E.A. and F.R.; supervision, S.Z. and D.D.; project administration, D.D. and M.C.-G. All authors have read and agreed to the published version of the manuscript.

Institutional Review Board Statement: Not applicable.

Informed Consent Statement: Not applicable.

Data Availability Statement: Data are available on request to the authors.

Conflicts of Interest: The authors declare no conflict of interest.

Abbreviations

The following abbreviations are used in this manuscript:

ACM	Active Connection Matrix
AWEI	Automated Water Extraction Index
DEM	Digital Elevation Model
dGPS	Differential Global Positioning System
EC	European Commission
EO	Earth Observation
EPSG	European Petroleum Survey Group
ESA	European Space Agency
GEE	Google Earth Engine
GNSS	Global Navigation Satellite System
GRD	Ground Range Detected
IW	Interferometric Wide
MNDWI	Modified Normalized Difference Water Index
NDVI	Normalized Difference Vegetation Index
NDWI	Normalized Difference Water Index

NIR	Near InfraRed
QGIS	Quantum Geographic Information System
S1	Sentinel-1
S2	Sentinel-2
SAR	Synthetic Aperture Radar
SAVI	Soil Adjusted Vegetation Index
SNAP	Sentinel Application Platform
SWAN	Simulating WAves Nearshore
SWIR	Short Wave InfraRed
UTM	Universal Transverse Mercator
WGS84	World Geodetic System 84
WI	Water Index

Appendix A. Graphical Comparison between the Results

In this appendix, the comparison between the mean distance and standard deviation for each date on S2 and S1 imagery considering all the algorithms is reported in graphic format. Figure A1 refers to the application of J-Net Dynamic and Canny on Sentinel-2 imagery in Castelldefels (Tables 3 and 5), while Figure A2 presents the same comparison but in S1 imagery (Tables 4 and 6). Figures A3 and A4 are related to Tables 3–6. They present the comparison between J-Net Dynamic and Canny on S2 and S1 in Somorrostro beach. The comparison between CoastSat both with automatic and manual threshold and J-Net Dynamic over MNDWI in Castelldefels is shown in Figure A5, while for Somorrostro it is shown in Figure A6 (Tables 8 and 7).
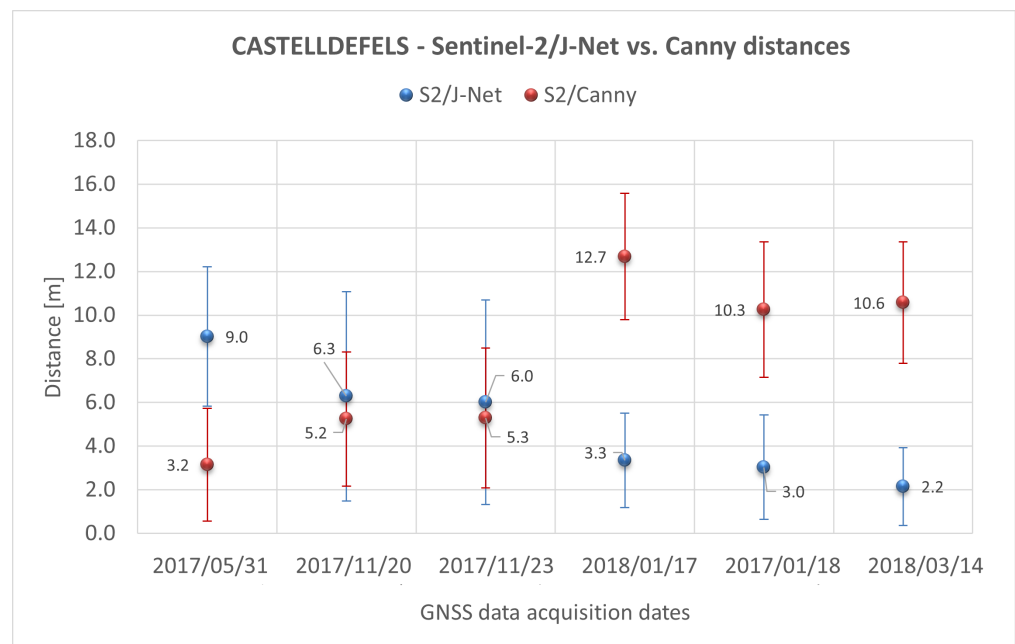
Figure A1. Comparison between the mean distance and standard deviation for each date on Sentinel-2 imagery considering J-Net Dynamic and Canny algorithms in Castelldefels.
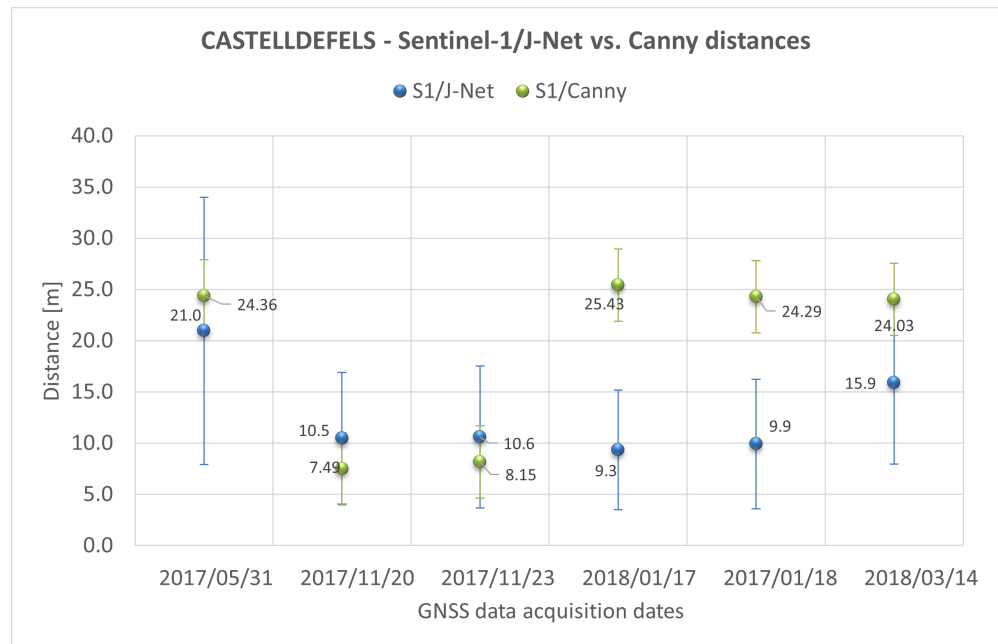
Figure A2. Comparison between the mean distance and standard deviation for each date on Sentinel-1 imagery considering J-Net Dynamic and Canny algorithms in Castelldefels.
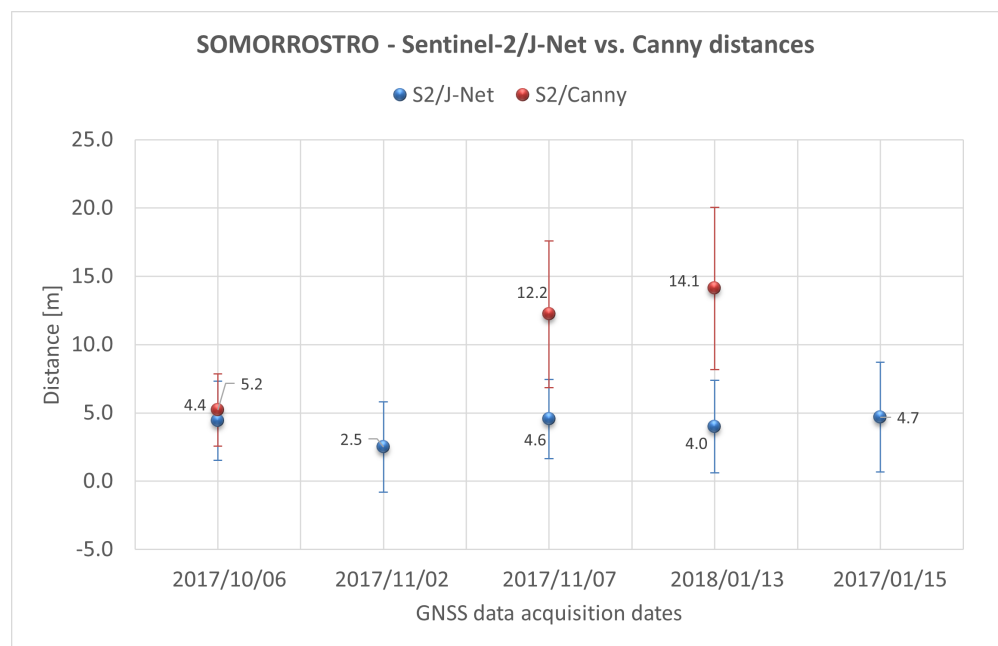

Figure A3. Comparison between the mean distance and standard deviation for each date on Sentinel-2 imagery considering J-Net Dynamic and Canny algorithms in Somorrostro.
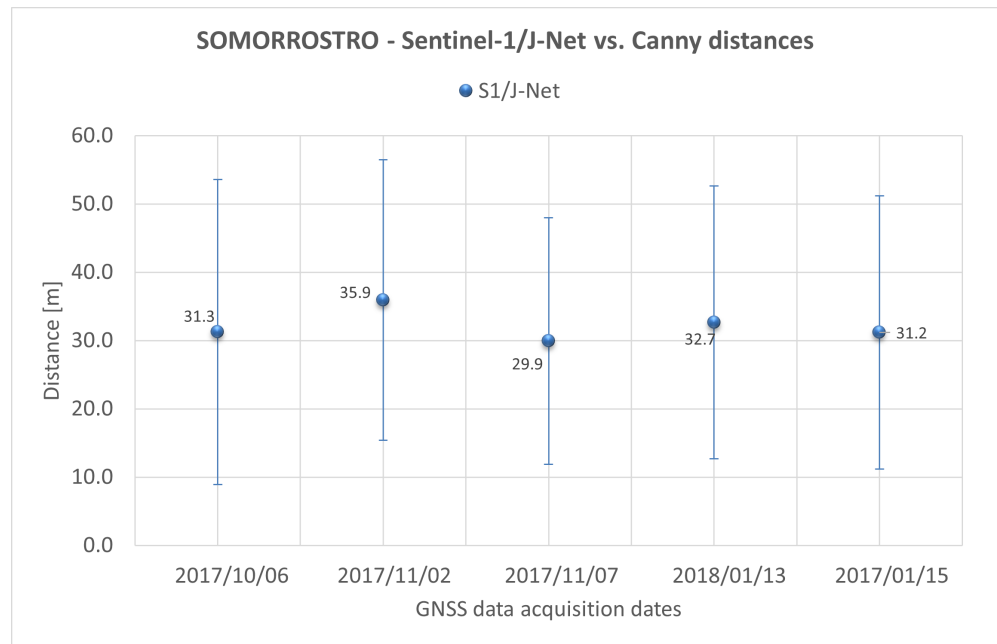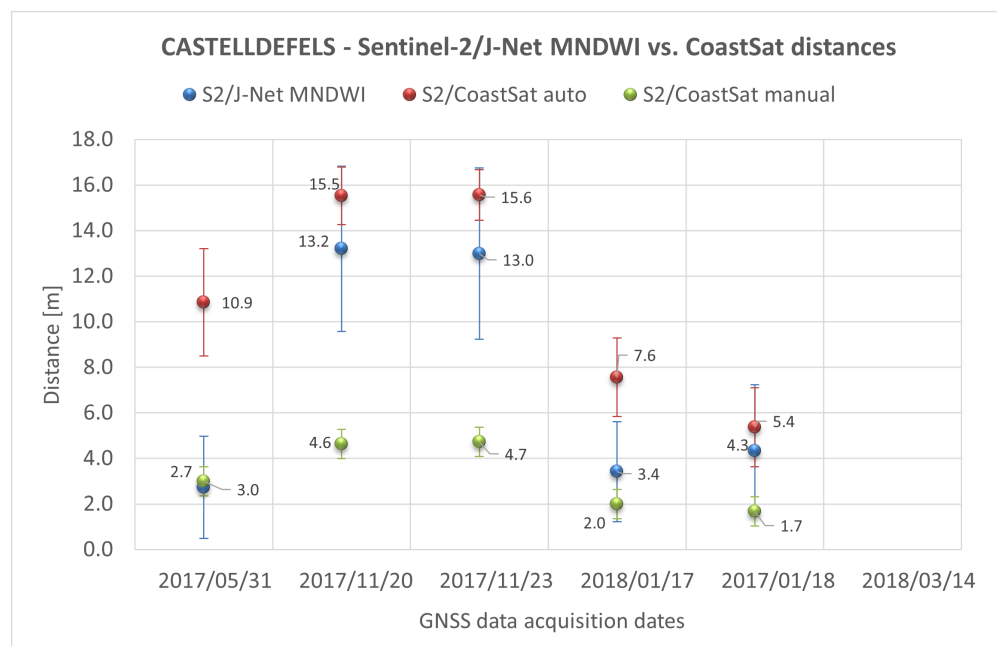
Figure A4. Comparison between the mean distance and standard deviation for each date on Sentinel-1 imagery considering J-Net Dynamic and Canny algorithms in Somorrostro.

Figure A5. Comparison between the mean distance and standard deviation for each date on Sentinel-2 imagery considering J-Net Dynamic plus MNDWI algorithm and CoastSat with automatic and manual thresholds in Castelldefels.
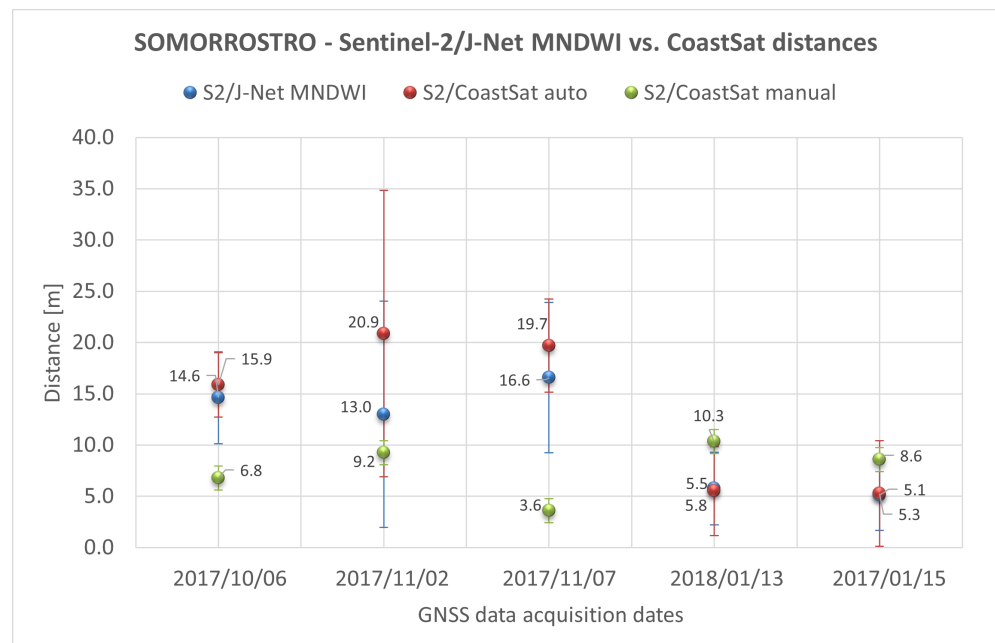
Figure A6. Comparison between the mean distance and standard deviation for each date on Sentinel-2 imagery considering J-Net Dynamic plus MNDWI algorithm and CoastSat with automatic and manual thresholds in Somorrostro.

References

1. Small, C.; Nicholls, R.J. A global analysis of human settlement in coastal zones. *J. Coast. Res.* **2003**, *19*, 584–599.
2. Rajib, S. Chapter 1—Global Coasts in the Face of Disasters. In *Coastal Management*; Krishnamurthy, R.R., Jonathan, M.P., Srinivasalu, S., Glaeser, B., Eds.; Academic Press: Cambridge, MA, USA, 2019; pp. 1–4. Available online: https://www.sciencedirect.com/science/article/pii/B9780128104736000017?via%3Dihub (accessed on 21 June 2022).
3. Neumann, B.; Vafeidis, A.T.; Zimmermann, J.; Nicholls, R.J. Future coastal population growth and exposure to sea-level rise and coastal ooding-a global assessment. *PLoS ONE* **2015**, *10*, e0118571. [CrossRef] [PubMed]
4. Oppenheimer, M.; Glavovic, B.C.; Hinkel, J.; Wal, R.v.; Magnan, A.K.; Abd-Elgawad, A.; Cai, R.; Cifuentes-Jara, M.; DeConto, R.M.; Ghosh, T.; et al. Sea Level Rise and Implications for Low-Lying Islands, Coasts and Communities. In *IPCC Special Report on the Ocean and Cryosphere in a Changing Climate*; Cambridge University Press: Cambridge, UK; New York, NY, USA, 2019; pp. 321–445. [CrossRef]
5. Frederikse, T.; Landerer, F.W.; Caron, L.; Adhikari, S.; Parkes, D.; Humphrey, V.; Dangendorf, S.; Hogarth, P.; Zanna, L.; Cheng, L.; et al. The causes of sea-level rise since 1900. *Nature* **2020**, *584*, 393–397. [CrossRef] [PubMed]
6. Mentaschi, L.; Vousdoukas, M.I.; Pekel, J.-F.; Voukouvalas, E.; Feyen, L. Global long-term observations of coastal erosion and accretion. *Sci. Rep.* **2018**, *8*, 12876. [CrossRef]
7. Jiménez, J.A.; Valdemoro, H.I. Shoreline evolution and its management implications in beaches along the Catalan coast. In *The Spanish Coastal Systems: Dynamic Processes, Sediments and Management*; Springer: Berlin/Heidelberg, Germany, 2019; pp. 745–764.
8. Pranzini, E.; Wetzel, L.; Williams, A.T. Aspects of coastal erosion and protection in Europe. *J. Coast. Conserv.* **2015**, *19*, 445–459. [CrossRef]
9. Boak, E.H.; Turner, I.L. Shoreline definition and detection: A review. *J. Coast. Res.* **2005**, *21*, 688–703. [CrossRef]
10. Pugliano, G.; Robustelli, U.; Di Luccio, D.; Mucerino, L.; Benassai, G.; Montella, R. Statistical deviations in shoreline detection obtained with direct and remote observations. *J. Mar. Sci. Eng.* **2019**, *7*, 137. [CrossRef]
11. Dominici, D.; Zollini, S.; Alicandro, M.; Della Torre, F.; Buscema, P.M.; Baiocchi, V. High Resolution Satellite Images for Instantaneous Shoreline Extraction Using New Enhancement Algorithms. *Geosciences* **2019**, *9*, 123. [CrossRef]
12. Gonçalves, G.; Duro, N.; Sousa, E.; Figueiredo, I. Automatic extraction of tide-coordinated shoreline using open source software and Landsat imagery. *Int. Arch. Photogramm. Remote Sens. Spat. Inf. Sci.* **2015**, *40*, 953. [CrossRef]
13. Pardo-Pascual, J.E.; Sánchez-García, E.; Almonacid-Caballer, J.; Palomar-Vázquez, J.M.; Priego De Los Santos, E.; Fernández-Sarría, A.; Balaguer-Beser, Á. Assessing the accuracy of automatically extracted shorelines on microtidal beaches from Landsat 7, Landsat 8 and Sentinel-2 imagery. *Remote Sens.* **2018**, *10*, 326. [CrossRef]
14. DaSilva, M.; Miot da Silva, G.; Hesp, P.A.; Bruce, D.; Keane, R.; Moore, C. Assessing Shoreline Change using Historical Aerial and RapidEye Satellite Imagery (Cape Jaffa, South Australia). *J. Coast. Res.* **2021**, *37*, 468–483. [CrossRef]
15. Wei, X.; Zheng, W.; Xi, C.; Shang, S. Shoreline Extraction in SAR Image Based on Advanced Geometric Active Contour Model. *Remote Sens.* **2021**, *13*, 642. [CrossRef]

16. Simarro, G.; Bryan, K.R.; Guedes, R.M.; Sancho, A.; Guillen, J.; Coco, G. On the use of variance images for runup and shoreline detection. *Coast. Eng.* **2015**, *99*, 136–147. [CrossRef]

17. Ribas, F.; Simarro, G.; Arriaga, J.; Luque, P. Automatic shoreline detection from video images by combining information from different methods. *Remote Sens.* **2020**, *12*, 3717. [CrossRef]

18. Vitousek, S.; Buscombe, D.; Vos, K.; Barnard, P.L.; Ritchie, A.; Warrick, J. The future of coastal monitoring through satellite remote sensing. *Camb. Prism. Coast. Futures* **2022**, *1*, e10. [CrossRef]

19. Braga, F.; Tosi, L.; Prati, C.; Alberotanza, L. Shoreline detection: Capability of COSMO-SkyMed and high-resolution multispectral images. *Eur. J. Remote Sens.* **2013**, *46*, 837–853. [CrossRef]

20. Dammann, D.O.; Eriksson, L.E.; Mahoney, A.R.; Eicken, H.; Meyer, F.J. Mapping pan-Arctic landfast sea ice stability using Sentinel-1 interferometry. *Cryosphere* **2019**, *13*, 557–577. [CrossRef]

21. Chaturvedi, S.K.; Banerjee, S.; Lele, S. An assessment of oil spill detection using Sentinel-1 SAR-C images. *J. Ocean Eng. Sci.* **2019**, *5*, 116–135. [CrossRef]

22. Wang, Y.; Wang, C.; Zhang, H. Combining a single shot multibox detector with transfer learning for ship detection using Sentinel-1 SAR images. *Remote Sens. Lett.* **2018**, *9*, 780–788. [CrossRef]

23. Forkuor, G.; Zoungrana, J.B.; Dimobe, K.; Ouattara, B.; Vadrevu, K.P.; Tondoh, J.E. Above-ground biomass mapping in West African dryland forest using Sentinel-1 and 2 datasets—A case study. *Remote. Sens. Environ.* **2020**, *236*, 111496. [CrossRef]

24. Steinhausen, M.J.; Wagner, P.D.; Narasimhan, B.; Waske, B. Combining Sentinel-1 and Sentinel-2 data for improved land use and land cover mapping of monsoon regions. *Int. J. Appl. Earth Obs. Geoinf.* **2018**, *73*, 595–604. [CrossRef]

25. Van Tricht, K.; Gobin, A.; Gilliams, S.; Piccard, I. Synergistic use of radar Sentinel-1 and optical Sentinel-2 imagery for crop mapping: A case study for Belgium. *Remote Sens.* **2018**, *10*, 1642. [CrossRef]

26. Montalti, R.; Solari, L.; Bianchini, S.; Del Soldato, M.; Raspini, F.; Casagli, N. A Sentinel-1-based clustering analysis for geo-hazards mitigation at regional scale: A case study in Central Italy. *Geomat. Nat. Hazards Risk* **2019**, *10*, 2257–2275. [CrossRef]

27. Thanh Noi, P.; Kappas, M. Comparison of random forest, k-nearest neighbor, and support vector machine classifiers for land cover classification using Sentinel-2 imagery. *Sensors* **2018**, *18*, 18. [CrossRef] [PubMed]

28. Drusch, M.; Del Bello, U.; Carlier, S.; Colin, O.; Fernandez, V.; Gascon, F.; Hoersch, B.; Isola, C.; Laberinti, P.; Martimort, P.; et al. Sentinel-2: ESA's optical high-resolution mission for GMES operational services. *Remote Sens. Environ.* **2012**, *120*, 25–36. [CrossRef]

29. Veloso, A.; Mermoz, S.; Bouvet, A.; Le Toan, T.; Planells, M.; Dejoux, J.-F.; Ceschia, E. Understanding the temporal behavior of crops using Sentinel-1 and Sentinel-2-like data for agricultural applications. *Remote Sens. Environ.* **2017**, *199*, 415–426. [CrossRef]

30. El Hajj, M.; Baghdadi, N.; Zribi, M.; Bazzi, H. Synergic use of Sentinel-1 and Sentinel-2 images for operational soil moisture mapping at high spatial resolution over agricultural areas. *Remote Sens.* **2017**, *9*, 1292. [CrossRef]

31. Demir, N.; Kaynarca, M.; Oy, S. Extraction of coastlines with fuzzy approach using SENTINEL-1 SAR image. *Int. Arch. Photogramm. Remote Sens. Spat. Inf. Sci.* **2016**, *41*, 747. [CrossRef]

32. Suhendra, S.; Setiawan, C.A.; Wibawa, T.A.; Borneo, B.B. Coastline change analysis on Bali island using Sentinel-1 satellite imagery. *Int. J. Remote Sens. Earth Sci. (IJReSES)* **2021**, *18*, 63–72. [CrossRef]

33. López-Caloca, A.A.; Monsiváis-Huertero, A.; López-Amaya, J. Sentinel-1 observation for shoreline delineation applied to Mexico's Coast. *Geocarto Int.* **2022**, *37*, 16462–16491. [CrossRef]

34. Vos, K.; Splinter, K.D.; Harley, M.D.; Simmons, J.A.; Turner, I.L. CoastSat: A Google Earth Engine-enabled Python toolkit to extract shorelines from publicly available satellite imagery. *Environ. Model. Softw.* **2019**, *122*, 104528. [CrossRef]

35. Almeida, L.P.; de Oliveira, I.E.; Lyra, R.; Dazzi, R.L.S.; Martins, V.G.; da Fontoura Klein, A.H. Coastal analyst system from space imagery engine (CASSIE): Shoreline management module. *Environ. Model. Softw.* **2021**, *140*, 105033. [CrossRef]

36. Sánchez-García, E.; Palomar-Vázquez, J.; Pardo-Pascual, J.; Almonacid-Caballer, J.; Cabezas-Rabadán, C.; Gómez-Pujol, L. An efficient protocol for accurate and massive shoreline definition from mid-resolution satellite imagery. *Coast. Eng.* **2020**, *160*, 103732. [CrossRef]

37. Pucino, N.; Kennedy, D.M.; Young, M.; Ierodiaconou, D. Assessing the accuracy of Sentinel-2 instantaneous subpixel shorelines using synchronous UAV ground truth surveys. *Remote Sens. Environ.* **2022**, *282*, 113293. [CrossRef]

38. McFeeters, S.K. The use of the normalized difference water index (NDWI) in the delineation of open water features. *Int. J. Remote Sens.* **1996**, *17*, 1425–1432. [CrossRef]

39. Xu, H. Modification of normalised difference water index (NDWI) to enhance open water features in remotely sensed imagery. *Int. J. Remote Sens.* **2006**, *27*, 3025–3033. [CrossRef]

40. Vos, K.; Harley, M.D.; Splinter, K.D.; Simmons, J.A.; Turner, I.L. Sub-annual to multi-decadal shoreline variability from publicly available satellite imagery. *Coast. Eng.* **2019**, *150*, 160–174. [CrossRef]

41. Feyisa, G.L.; Meilby, H.; Fensholt, R.; Proud, S.R. Automated water extraction index: A new technique for surface water mapping using landsat imagery. *Remote Sens. Environ.* **2014**, *140*, 23–35. [CrossRef]

42. Fisher, A.; Flood, N.; Danaher, T. Comparing landsat water index methods for automated water classification in eastern Australia. *Remote Sens. Environ.* **2016**, *175*, 167–182. [CrossRef]

43. Ferrentino, E.; Buono, A.; Nunziata, F.; Marino, A.; Migliaccio, M. On the use of multipolarization satellite SAR data for coastline extraction in harsh coastal environments: The case of Solway Firth. *IEEE J. Sel. Top. Appl. Earth Obs. Remote Sens.* **2020**, *14*, 249–257. [CrossRef]

44. Zollini, S.; Alicandro, M.; Cuevas-González, M.; Baiocchi, V.; Dominici, D.; Buscema, P.M. Shoreline extraction based on an active connection matrix (ACM) image enhancement strategy. *J. Mar. Sci. Eng.* **2020**, *8*, 9. [CrossRef]
45. Kelly, J.; Gontz, A. Using GNSS-surveyed intertidal zones to determine the validity of shorelines automatically mapped by Landsat water indices. *Int. J. Appl. Earth Obs. Geoinf.* **2018**, *65*, 92–104.
46. Maglione, P.; Parente, C.; Vallario, A. High resolution satellite images to reconstruct recent evolution of domitian coastline. *Am. J. Appl. Sci.* **2015**, *12*, 506. [CrossRef]
47. ESA—European Space Agency (n.d.). Sentinel-1—Overview—Sentinel Online. Available online: https://sentinel:esa:int/web/sentinel/missions/sentinel-1/overview (accessed on 19 May 2020).
48. ESA—European Space Agency (n.d.). Sentinel-2—Overview—Sentinel Online. Available online: https://sentinel:esa:int/web/sentinel/missions/sentinel-2/overview (accessed on 21 May 2020).
49. Lee, J.; Jurkevich, L.; Dewaele, P.; Wambacq, P.; Oosterlinck, A. Speckle filtering of synthetic aperture radar images: A review. *Remote Sens. Rev.* **1994**, *8*, 313–340. [CrossRef]
50. Lopes, A.; Nezry, E.; Touzi, R.; Laur, H. Structure detection and statistical adaptive speckle filtering in SAR images. *Int. J. Remote Sens.* **1993**, *14*, 1735–1758. [CrossRef]
51. Wang, P.; Zhang, H.; Patel, V.M. SAR image despeckling using a convolutional neural network. *IEEE Signal Process. Lett.* **2017**, *24*, 1763–1767. [CrossRef]
52. Sivaranjani, R.; Roomi, S.; Senthilarasi, M. Speckle noise removal in SAR images using Multi-Objective PSO (MOPSO) algorithm. *Appl. Soft Comput.* **2019**, *76*, 671–681. [CrossRef]
53. Buscema, P.M. *Sistemi ACM e Imaging Diagnostico: Le Immagini Mediche Come Matrici Attive di Connessioni*; Springer Science & Business Media: New York, NY, USA, 2006.
54. Buscema, M.; Catzola, L.; Grossi, E. Images as active connection matrixes: The J-net system. *Int. J. Intell. Comput. Med. Sci. Image Process.* **2008**, *2*, 27–53. [CrossRef]
55. Buscema, M.; Grossi, E. J-Net System: A New Paradigm for Artificial Neural Networks Applied to Diagnostic Imaging. In *Applications of Mathematics in Models, Artificial Neural Networks and Arts*; Publishing House: Dordrecht, The Netherlands, 2010; pp. 431–455.
56. Canny, J. A computational approach to edge detection. *IEEE Trans. Pattern Anal. Mach. Intell.* **1986**, *6*, 679–698. [CrossRef]
57. Sahir, S. Canny Edge Detection Step by Step in Python—Computer Vision. 2019. Available online: https://towardsdatascience:com/canny-edge-detection-step-by-step-in-python-computer-vision-b49c3a2d8123 (accessed on 10 October 2020).
58. Github CoastSat. Available online: https://github.com/kvos/CoastSat (accessed on 16 November 2022).
59. Castelle, B.; Masselink, G.; Scott, T.; Stokes, C.; Konstantinou, A.; Marieu, V.; Bujan, S. Satellite-derived shoreline detection at a high-energy meso-macrotidal beach. *Geomorphology* **2021**, *383*, 107707. [CrossRef]
60. Sancho-García, A. Beach Inundation and Morphological Changes during Storms Using Video Monitoring Techniques. Ph.D. Thesis, Universitat Politècnica de Catalunya, Barcelona, Spain, 2012. Available online: https://digital.csic.es/handle/10261/93449 (accessed on 10 December 2022).
61. De Swart, R.L.; Ribas, F.; Calvete, D.; Simarro, G.; Guillén, J. Observations of megacusp dynamics and their coupling with crescentic bars at an open, fetch-limited beach. *Earth Surf. Proc. Land* **2022**, *47*, 3180–3198. [CrossRef]
62. Mendoza, E.T.; Jimenez, J.A.; Mateo, J. A coastal storms intensity scale for the Catalan sea (NW Mediterranean). *Nat. Hazards Earth Syst. Sci.* **2011**, *11*, 2453–2462. [CrossRef]